

An Old Supernova Remnant within an HII Complex at $\ell \approx 173^\circ$: FVW 172.8+1.5

Ji-hyun Kang^{1,3,4}, Bon-Chul Koo², and Chris Salter¹

¹*Arecibo Observatory, HC 3 Box 53995, Arecibo, PR 00612*

²*Department of Physics and Astronomy, Seoul National University, Gwanak 599
Gwanak-ro, Gwanak-gu, Seoul 151-742, Korea*

³*Yonsei University, 50 Yonsei-ro, Seodaemun-gu, Seoul 120-749, Korea*

⁴*Korea Astronomy and Space Science Institute 776, Daedeokdae-ro, Yuseong-gu, Daejeon
305-348, Korea*

jkang@kasi.re.kr, koo@astro.snu.ac.kr, csalter@naic.edu

ABSTRACT

We present the results of HI 21-cm line observations to explore the nature of the high-velocity (HV) HI gas at $\ell \sim 173^\circ$. In low-resolution HI surveys this HV gas appears as faint, wing-like, HI emission that extends to velocities beyond those allowed by Galactic rotation. We designate this feature FVW (Forbidden Velocity Wing) 172.8+1.5. Our high-resolution (3.'4) Arecibo HI observations show that FVW 172.8+1.5 is composed of knots, filaments, and ring-like structures distributed over an area a few degrees in extent. These HV HI emission features are confined within the limits of the HII complex G173+1.5, which is composed of five Sharpless HII regions distributed along a radio continuum loop of size $4^\circ.4 \times 3^\circ.4$, or $\sim 138 \text{ pc} \times 107 \text{ pc}$, at a distance of 1.8 kpc. G173+1.5 is one of the largest star-forming regions in the outer Galaxy. We demonstrate that the HV HI gas is well correlated with the radio continuum loop and that the two seem to trace an expanding shell. The expansion velocity of the shell is large (55 km s^{-1}) suggesting that it represents a supernova-remnant (SNR). We derive physical parameters for the shell and show these to be consistent with the object being a SNR. We also detect hot X-ray emitting gas inside the HII complex by analyzing the ROSAT all-sky X-ray background survey data. This also supports the SNR interpretation. We conclude that the HV HI gas and the X-rays are most likely the products of a supernova explosion(s) within the HII complex, possibly in a cluster that triggered the formation of these HII regions.

Subject headings: supernova remnants — ISM: individual (FVW172.8+1.5) — radio lines: ISM — ISM: HII regions — stars: formation

1. Introduction

In large-scale (ℓ, v) diagrams of HI 21-cm line emission in the Galactic plane, there are many small, faint, high-velocity “wing-like” features extending to velocities well beyond the maximum or minimum permitted by Galactic rotation (Koo & Kang 2004). These “Forbidden Velocity Wings (FVWs)” are likely due to energetic phenomena in the Galaxy, as they are confined to small areas ($\lesssim 2^\circ$), and project smoothly beyond the general Galactic emission to high velocities. Koo & Kang (2004) suggested that some of these FVWs may represent the expanding shells of “missing” supernova remnants (SNRs), which are not included in existing SNR catalogs. The basic idea is that old SNRs are faint in the radio continuum, making it difficult to identify them because of both the confusion due to the Galactic background emission, and observational limitations (e.g., Brogan et al. 2006). Koo & Kang (2004) considered the fact that an old SNR should possess a fast-expanding HI shell that will still be present as a coherent entity after the remnant becomes too faint to be visible in the radio continuum. If its expansion velocity is greater than the minimum or maximum velocities permitted by Galactic rotation, then an old SNR shell, or part of it (maybe the caps), could be detected as high-velocity HI gas, e.g., FVWs. Indeed, Koo et al. (2006) have carried out high-resolution HI line observations toward one FVW and detected a rapidly expanding (80 km s^{-1}) HI shell, the parameters of which are consistent with those of the remnant of a SN that exploded some 0.3 Myr ago.

Recently, Kang & Koo (2007) identified 87 FVWs from the Leiden/Dwingeloo HI survey (LDS; Hartmann & Burton 1997) and the Southern Galactic Plane Survey data (SGPS; McClure-Griffiths et al. 2005). Among these, 6 FVWs are found to be coincident with SNRs, 4 with nearby galaxies, and 3 with high-velocity clouds. The rest (85%) are not associated with any obvious objects that could be responsible for their high velocities. We have since been making follow-up high-resolution HI observations of these FVWs of unknown nature using the Arecibo 305-m and Green Bank 100-m radio telescopes in order to identify their natures and origins, and have now observed $\sim 30\%$ of them. We find that about 40% of the observed FVWs have shell-like morphologies. More than half of these are apparently expanding at $\gtrsim 50 \text{ km s}^{-1}$, which supports the possibility of some FVWs being old SNRs. The other 60% show irregular structures consisting of filaments and clumps. Most of these show faint bumps in their line profiles indicating high-velocity HI clouds. They might correspond to the fast-moving, compact clouds in the disk, or in the disk-halo interface, that have been recently detected in sensitive, high-resolution HI surveys (Stanimirović et al. 2006; Begum et al. 2010, and references therein). The full results from our survey will be presented in a separate paper.

Here, we report Arecibo HI 21-cm line observations of FVW172.8+1.5. This particular

FVW is unique in that it is associated with an HII complex in the outer Galaxy. We show that FVW 172.8+1.5 is most likely an old SNR produced in this complex. The catalog of Kang & Koo (2007) lists this feature as two objects, FVW173.0+0.0 and FVW173.0+3.0. However, the Arecibo HI image shows that these are likely to be parts of a single coherent object, which we will call FVW172.8+1.5. In Section 2, we describe the HI observations. The HI results are presented in Section 3. In Section 4, we present a multi-wavelength view of the HII complex in this region and investigate its association with FVW 172.8+1.5. We discuss the origin of FVW172.8+1.5 and the star-formation history in this area in Section 5, presenting a summary in Section 6.

2. The HI 21-cm Line Observations

HI 21-cm line observations of FVW172.8+1.5 were made in 2006 October with the Arecibo 305-m telescope using the 7-beam, dual-polarization, Arecibo L-band Feed Array (ALFA). The beam-to-beam spacing for the scanning pattern used was $1'.8$. GALSPECT, a dedicated spectrometer for Galactic HI ALFA surveys, was used as the backend. Both wide- and narrow-band spectra were acquired (see Stanimirović et al. 2006, for details). Here we present data from the narrower 7.14-MHz band, which is analyzed into 8192 equally spaced channels, giving an unsmoothed velocity resolution of 0.18 km s^{-1} .

The field observed covers an area of 7.5×4.5 centered at $(\alpha, \delta) = (5^{\text{h}}37^{\text{m}}, 35^{\circ}40')$ (J2000). The observations employed the basket-weaving technique (Peek & Heiles 2008; Peek et al. 2007), which scans the sky with a zig-zag pattern by driving the telescope up and down on the prime meridian at a speed of 1.5 arcmin/sec. For bandpass correction, a “Least-Squares Frequency Switching” (LSFS; Heiles 2007) calibration was performed each day. Data reduction used the IDL pipe-line codes developed by the Berkeley group (Peek & Heiles 2008). Using these, the data are converted into a brightness temperature cube. The contamination due to the coma sidelobes of the ALFA off-centre beams has been corrected (see Peek & Heiles 2008, for the details of data reduction). The final cube has a velocity resolution of 0.74 km s^{-1} , a spatial HPBW of 3.4 arcmin, and an rms of 0.13 K.

3. The HI Results

Fig. 1 shows channel images of the Arecibo HI data. The HI emission associated with FVW172.8+1.5 is visible for $+19.5 \text{ km s}^{-1} \lesssim v_{\text{LSR}} \lesssim +50.4 \text{ km s}^{-1}$. At the highest velocities ($+40.1 \text{ km s}^{-1} \lesssim v_{\text{LSR}} \lesssim +50.4 \text{ km s}^{-1}$), the HI appears to be largely separated into two con-

centrations centered at $\sim (5^{\text{h}}37^{\text{m}}, +36^{\circ}30')$ and $\sim (5^{\text{h}}27^{\text{m}}, +34^{\circ}30')$, These were previously designated FVW173.0+3.0 and FVW173.0+0.0 respectively. The northern concentration (FVW173.0+3.0) looks diffuse and clumpy, and appears to form a ring-like structure with a diameter of $\sim 2^{\circ}$. In contrast, the southern concentration (FVW173.0+0.0) appears to be confined to a few small ($\lesssim 30'$) regions. At lower velocities ($+16.6 \text{ km s}^{-1} \lesssim v_{\text{LSR}} \lesssim +35.0 \text{ km s}^{-1}$), a thin, filamentary feature that surrounds the two concentrations appears, so that the entire structure appears to be a large shell with an extent of $4^{\circ}.4 \times 3.4^{\circ}$. The crosses in Fig. 1 and the ellipse superposed on the $+24.7 \text{ km s}^{-1}$ channel map mark the approximate center and boundary of the shell structure. At $+14.4 \text{ km s}^{-1}$ and lower velocities, the HI emission from the Galactic ISM dominates, so that no particular HI feature associated with the source is recognizable (see also § 4.1.1).

The various HI features described above are also visible in Fig. 2, which is a three-color image of the HI gas integrated over different velocity intervals. In this figure, we superpose the Effelsberg 11-cm radio continuum contours (Fürst et al. 1990). It is seen that the high-velocity HI emission features lie essentially within the radio continuum filaments. The northwestern high velocity HI gas, represented by red and green colors, are confined within the northern part of the continuum structure, while the HI features at lower velocities (colored blue) lie along the inner boundary of the outer radio continuum filaments. The morphological relation between the HI and the radio filaments strongly suggests their association. In addition, there is little possibility of chance alignment of the two structures, because confusion is low along the line of sight in the direction of $\ell \sim 173^{\circ}$. The increase of the surface area and/or the size of the HI -emitting region with decreasing velocity suggests that we are looking at the receding portion of an expanding shell. The HI morphology does not exactly match that of a uniformly expanding spherical shell, but this could be due to a non-uniform and inhomogeneous ambient interstellar medium. The radio continuum structure is part of the HII complex in this area, and we will investigate the association of the two at other wavelengths in Section 4 and their physical properties and origin in Section 5.

The velocity structure of the high-velocity HI features is shown in Fig. 3, which shows the peak HI brightness temperature in Galactic longitude as a function of Galactic latitude and velocity. This position-velocity diagram shows the high-velocity gas over the entire field in a single diagram and enhances the appearance of small-scale wing-like features. Fig. 3 shows that FVW172.8+1.5 is composed of many small-scale, high-velocity wings spatially confined to $-1^{\circ} < b < +4^{\circ}$, which suggests an inhomogeneous nature for the shell. These wings are mostly straight but some have the shape of an extended ring, e.g., that at $b = -0.2^{\circ}$. This indicates that the shell is composed of small clumps. Since only the high-velocity end portions of the wings are visible, their central velocities are usually not accessible. However, a few line profiles in the area near $(5^{\text{h}}34.5^{\text{m}}, +36^{\circ}03')$ show discrete spectral features at high velocities

(Fig. 4). A Gaussian fit to these features results in a central velocity of $+33 - +35 \text{ km s}^{-1}$ and a velocity dispersion of $4.3 - 6.4 \text{ km s}^{-1}$, corresponding to kinetic temperatures of $2,200 - 4,900 \text{ K}$ if the broadening is entirely due to thermal motions.

4. The $\ell = 173^\circ$ region in Multi Wavebands

4.1. Radio Continuum

4.1.1. The HII Complex G173+1.5

The region of Auriga within which FVW172.8+1.5 lies is an HII complex composed of Sharpless HII regions and OB associations in the Perseus arm (Fig. 5). The HII regions are organized along a large ($\sim 7^\circ \times 4^\circ$) filamentary structure resembling a bow tie (Kerton et al. 2007). The HII regions have been studied previously (e.g. Israel & Felli 1978), and they are largely at two different distances (see Table 1). To the northeast of the structure, S231, S232, S233, and S235 are known to be associated with a giant molecular cloud at a distance of 1.8 kpc (Evans & Blair 1981), with CO radial velocities of -18.1 to -23.0 km s^{-1} (Blitz et al. 1982), in which active star formation is on-going (see § 4.3). The distances determined by spectrophotometry of the exciting stars of individual HII regions range from 1.0 to 2.3 kpc, but the distance to the associated molecular cloud (1.8 kpc) is often adopted as the distance to the whole HII complex. To the south of the complex, two 1° -sized HII regions S229 (IC 405) and S236 (IC 410) and the large ($\sim 5^\circ$) diffuse HII region S230 are present. S236 is associated with a molecular cloud at -7.2 km s^{-1} and might be at a considerably greater distance because the estimated distance to its central star cluster (NGC 1893) ranges from 3.2 to 6 kpc (Sharma et al. 2007, and references therein). For the other two HII regions (S229 and S230), not much has been known, although Fich et al. (1990) measured $\text{H}\alpha$ velocities of $+4.4$ and 0.0 km s^{-1} toward S229 and S230, respectively. Toward S229, CO $J = 1-0$ emission at $+6.7 \text{ km s}^{-1}$ has been detected, but it may not be related to the HII region (Blitz et al. 1982). The small HII regions S234 (IC 417) and S237 in the middle of the “bow-tie” have velocities of -13 and -4 km s^{-1} , similar to the first and second groups respectively. A recent photometric determination of the distance to the central cluster (Stock 8) of S234 also agrees with the distance to the northwestern group of HII regions, i.e., $2.05 \pm 0.10 \text{ kpc}$ (Jose et al. 2008). We therefore consider that the Sharpless HII regions S231–S235 form the active star formation complex G173+1.5 at a distance of 1.8 kpc at $v_{\text{LSR}} \approx -20 \text{ km s}^{-1}$. The other HII regions have considerably different velocities and distances, and they are not considered to be associated with this complex.

The morphology of the region suggests an association between the large radio continuum

filamentary structures and the HII regions. Filaments A through D (see Fig. 5) have similar concave shapes suggesting that they have resulted from a common source within the HII complex. For the radio filament A, we have found an HI filamentary structure along the radio feature at $v_{\text{LSR}} = -25$ to -28 km s $^{-1}$ (Fig. 6). The correlation is not perfect in the sense that the HI feature looks less curved than the continuum filament and seems to extend outside of the field shown in Fig. 6. However, the velocity is close to the CO velocity of S232, and the two could be associated. We could not find any HI structures associated with the other continuum filaments. Filament E has an enhanced brightness and its curvature is opposite to those of Filaments A–D. It is likely that the enhanced brightness and the convex shape is due to interaction with a dense ambient medium there, although no responsible molecular cloud is seen in the available CO survey data (Dame et al. 2001, see also Fig. 9). Hence, filaments A–E are likely to be associated with the HII complex G173+1.5, although we have only circumstantial evidence, except perhaps for filament A. Kinematic evidence is needed to confirm the association.

4.1.2. *The Radio Continuum Spectrum of Filament A*

The nature of the radio emission from the large continuum filamentary structure has been discussed previously, although not in detail. Kerton et al. (2007) noted this structure in the 1420 MHz Canadian Galactic Plane Survey map, and argued that the filaments D & E are thermal emission based on either the presence of corresponding infrared emission and/or the rising spectrum between 408 and 1420 MHz. Gao et al. (2010) claim that filament A shows a thermal spectrum between the higher frequencies of 1.4 and 5 GHz.

Using radio continuum data from 325 MHz to 2.7 GHz available on the web (Table. 2), we have attempted a study of the continuum spectrum of the filaments associated with the structure. The faint filamentary features are visible at most of these frequencies. Here we will focus on Filament A at $(\ell, b) \sim (172^{\circ}5, +3^{\circ}5)$, which stands out at 325 MHz in WENSS. To estimate values of spectral index, we (1) converted the WENSS data to brightness temperature, thus bringing all surveys to the same intensity units, (2) convolved all images to have a circular beam of FWHM = $4'.7$, the declination beam size of the CGPS 408 MHz image at $\delta = 37^{\circ}$, (3) gridded the images onto the $2'$ -spaced pixels of the Effelsberg data, and (4) subtracted out all point sources. The final images are shown in Fig. 7, where the dotted and solid boxes mark Filament A and the HII region, S232, which provides a reference with a thermal spectrum. Finally, we removed a smooth, linear, large-scale background emission gradient using two neighboring areas, marked by pairs of boxes flanking the HII region and the filament in Fig. 7.

The continuum spectra of Filament A and S232 are shown in Fig. 8 (left) by filled and open circles respectively. The total flux densities are given in Table 3. The error bars in Fig. 8 represent standard deviations in the neighboring areas after removal of smooth backgrounds. Using all flux density values from 325 to 2695 MHz, the estimated spectral index ($S_\nu \propto \nu^{-\alpha}$) of S232 is $\alpha = -0.09 \pm 0.02$, while that of Filament A is $\alpha = +0.23 \pm 0.06$. We also derived spectral indices for Filament A and S232 using T-T plots (Turtle et al. 1962). The regions used for making the T-T plots are those over which the total flux densities were derived. Fig. 8 (right) shows a T-T plot between 325 and 2695 MHz of Filament A. The points are well described by a linear fit. The slopes of the plots, and the values of α derived between different pairs of frequencies, are summarized in Table 4. For S232, the derived spectral indices are consistent, ranging from $\alpha = -0.04$ to $+0.09$ which, together with the total flux density spectral index of $\alpha = -0.09$, is reasonably close to the value of $\alpha = +0.1$ expected for an optically thin thermal source. However, the spectral indices derived for Filament A are not straightforward to interpret. The frequency pairs that include 325 MHz result in $\alpha = +0.50 \pm 0.11$ and $+0.32 \pm 0.06$, consistent with non-thermal emission, while the pairs that include 408 MHz yield $\alpha = +0.07 \pm 0.10$ and -0.04 ± 0.08 , compatible with thermal emission. These trends are consistent with the plot of the total flux densities (Fig. 8 left). In that plot, if either the 325 MHz or the 408 MHz data point is excluded, then the spectral index of Filament A would respectively be flatter or steeper than the $\alpha = +0.23 \pm 0.06$ derived using data at all frequencies.

As mentioned at the beginning of this section, previous studies claimed that the radio emission from some of these filaments is of thermal origin. However, our analysis in this section indicates the presence of a non-thermal component in filament A. The fact that the spectral index of S232, as derived from the same data, is consistent with optically-thin thermal emission supports our result. Therefore, it is more likely that the filament has both thermal and non-thermal components (see also § 4.3). If thermal and non-thermal components co-exist in the filament, a steep spectrum at lower frequencies, and a flat spectrum at higher frequencies (as found by Gao et al.), might be expected. Also, if thermal and non-thermal components co-exist in the continuum emission of Filament A, this could be the case for Filaments B–E. We have examined the polarization maps of this area. The G173 complex region was covered by the polarization surveys at 1.4 and 5 GHz (Landecker et al. 2010; Gao et al. 2010). While the 1.4 GHz polarization data of Landecker et al. do not show any apparent counterparts to the G173 structure, the 5 GHz polarization data of Gao et al. do show some filamentary features associated with the structure. In the polarized intensity map of Gao et al. (their Fig. 17), two depolarized filaments, indicating a thermal nature, are recognizable; one at $(\ell, b) \sim (174.3, +2.0)$, which corresponds to Filament B, and the other at $\sim (171.0, +2.5)$, located between Filaments A and D. Other than B, the

continuum filaments have no apparent counterparts in this image. Hence, it is difficult to discuss the nature of Filaments A - E using the current polarization data, with the exception that a thermal component appears to dominate in Filament B. The nature of the continuum filaments needs to be investigated with more sensitive full-Stokes continuum data.

4.2. X-rays

In the *ROSAT Survey Diffuse X-ray Background Map* (Snowden et al. 1997), there is faint, extended X-ray emission projected against the HII complex G173+1.5. (Fig. 9, top frames). The emission is mainly from two regions, one within the S231-235 complex and the other associated with S229/S236. The emission is not visible in the soft band (1/4 keV) but appears at the hard bands (3/4 and 1.5 keV). This is consistent with the emission being associated with G173+1.5 because if we adopt $A_V = 1.2$ mag (or $N(H) = 2.3 \times 10^{21}$ cm $^{-2}$) corresponding to the extinction to S234 (Jose et al. 2008) as the extinction to G173+1.5, the transmission of 1/4 keV photons is essentially zero ($\lesssim 10\%$) while it is 40% and 80% at 3/4 and 1.5 keV, respectively (Seward 2000). The emission is not uniform and the ratio of 1.5 to 3/4 keV intensities vary over the field. Note that, since the contributions from point sources have been removed from the map, the emission is from diffuse sources, although some compact sources might have been included, e.g., the bright spot near S234. For the present analysis, we simply derive the X-ray photon counts inside the solid ellipse marked in Fig.9. The background is estimated from the surrounding regions marked by the two dotted ellipses. The derived count rates over 8.8 deg 2 are 0.76 ± 0.08 cts s $^{-1}$ and 0.78 ± 0.11 cts s $^{-1}$ in 3/4 keV and 1.5 keV bands, respectively. The ratio of 1.5 keV to 3/4 keV is 1.0 ± 0.2 . Using the model of Snowden et al. (1997), the ratio corresponds to either a power-law photon spectrum ($E^{-\alpha}$, where E is energy) of index $\alpha \sim 4$ or thermal spectrum with temperature of $\sim 10^{6.9}$ K for $N(H) = 2.3 \times 10^{21}$ cm $^{-2}$. The power-law index 4 is considerably steeper than that of a pulsar wind nebula, e.g., ~ 2 for the Crab nebula, so that we may rule out a non-thermal origin. The diffuse extended morphology also supports a thermal origin. According to Snowden et al. (1997), the attenuated count rate of thermal X-ray emission from $10^{6.9}$ K gas at 3/4 keV is ~ 0.01 cts s $^{-1}$ arcmin $^{-2}$ for an emission measure of 1 cm $^{-6}$ pc. Therefore, the observed average 3/4 keV-band count rate of 2.4×10^{-5} cts s $^{-1}$ arcmin $^{-2}$ implies an average emission measure of 0.0024 cm $^{-6}$ pc. If we use $4R/3$, where $R = 60$ pc is the geometrical mean radius of the shell, as the mean depth along the line of sight, the mean electron density is about 5.5×10^{-3} cm $^{-3}$. This implies a thermal energy for the X-ray emitting gas of $\sim 3 \times 10^{50}$ ergs, assuming that it fills the entire interior of the shell. If instead the X-ray emitting gas fills only parts of the shell interior, then the thermal energy will be somewhat smaller than this. The derived thermal energy is close to that of an old SNR,

which, together with the high temperature, suggests that the hot gas might have originated from an SN explosion within the HII complex G173+1.5.

4.3. H α and CO

The radio continuum structure of G173+1.5 has counterparts in H α . Fig. 9 (bottom left) is the H α full-sky map (6' FWHM resolution) composite of the Virginia Tech Spectral line Survey (VTSS), the Southern H α Sky Survey Atlas (SHASSA), and the Wisconsin H-Alpha Mapper (WHAM) survey (Finkbeiner 2003). In the northern area covered by the VTSS H α image (Dennison et al. 2000) delicate H α filaments are clearly visible, well correlated with the radio continuum filaments. If we compare in detail, however, there is a slight shift between the radio and H α filaments; the H α emission peaks at slightly lower latitudes, i.e. slightly inside, the complex (Fig. 10). If the radio feature is due to thermal emission, the ratio of the two intensities are roughly constant as both depend on the emission measure. Using the formulae given in Spitzer (1978), the H α intensity from ionized gas at 10,000 K is given by $I(H\alpha) \approx 0.36(n_p/n_e)EM$ Rayleigh (R) where $EM = \int n_e^2 ds$ (cm^{-6} pc), and n_p and n_e are proton and electron densities, respectively. The corresponding radio brightness temperature at 11 cm, using the formulae from Draine (2011), is $T_b \approx 0.40 \times 10^{-3}(n_p/n_e)EM$ K. Therefore, we have $T_b/I(H\alpha) \approx 4 \times 10^{-3}$ K R $^{-1}$ adopting an extinction of $A_V = 1.4$ mag. At $T = 5,000$ K, this ratio would be slightly lower. Since the H α intensity is normalized by 20 R and the 11-cm brightness is normalized by 0.1 K, the thermal 11-cm emission would have a comparable (~ 0.8) normalized intensity in Fig. 10. In fact, Fig. 10 shows that at the H α peak positions this is indeed the case. On the other hand, at the radio continuum maxima, the 11-cm brightness is considerably greater than the H α intensity, which implies a non-thermal origin. Therefore, the 11-cm continuum emission appears to be composed of both thermal and non-thermal components, which is consistent with our conclusion from the previous section.

Figure 9 (bottom right) show the CO J=1-0 intensity map integrated over $v_{\text{LSR}} = -25$ to -15 km s $^{-1}$ (Dame et al. 2001). There is one giant molecular cloud at $(\ell, b) \sim (173.^{\circ}5, 2.^{\circ}5)$. Four HII regions, S231, S232, S233, and 235, are clustered around this molecular cloud. CO observations of this cloud show close positional correlations between the optical HII regions and the molecular cloud (Heyer et al. 1996). The giant molecular cloud appears as interconnected filaments with bright CO emission located at the projected optical edges of S235 and S232. S233 lies within a void in the CO emission, implying complete ionization and photodissociation of the molecular material. It has been known that active star formation is ongoing around these HII regions, and that jets and outflows from young stellar objects

have been observed in molecular lines (e.g., Shepherd & Watson 2002; Beuther et al. 2002).

5. Discussion

5.1. The Origin of FVW172.8+1.5

Our results indicate that the fast-moving HI gas in FVW172.8+1.5 is confined within the HII complex G173+1.5 and has good spatial correlation with the radio continuum structure. This strongly suggests its origin lies within the complex. Morphological association between the HI emission and the continuum/H α filaments further suggests that they probably trace the same object, i.e., an expanding shell. The X-rays detected within the complex may also be associated with this shell. In this section, we first derive the parameters that an expanding shell would possess, and then explore its possible origin. We take the systemic velocity and distance of both the HII complex and FVW172.8+1.5 to be $v_{\text{sys}} \approx -20 \text{ km s}^{-1}$ and 1.8 kpc.

5.1.1. The parameters of FVW172.8+1.5 as an expanding shell

The total extent of the putative shell based on the radio continuum filaments and our HI observations is $4^{\circ}.4 \times 3^{\circ}.4$, which converts to $138 \text{ pc} \times 107 \text{ pc}$ at 1.8 kpc. If we adopt the velocity centers of the highest-velocity clumps given in § 4 ($+35 \text{ km s}^{-1}$) as an endcap velocity of the shell, its expansion velocity is 55 km s^{-1} . To derive the total HI mass and kinetic energy of the FVW172.8+1.5, we need to estimate the *total* mass of the expanding shell. This can be done by extrapolating the mass distribution we derive for high velocities. Fig. 11 shows the distribution of HI mass in each 2.2 km s^{-1} velocity interval between $v_{\text{LSR}} = +14$ and $+46 \text{ km s}^{-1}$. We assume the receding and approaching hemispheres of the expanding shell to be symmetric and centered at $v_{\text{LSR}} = -20 \text{ km s}^{-1}$. Note that the approaching portion of the shell is not visible because of confusion by the Galactic background/foreground HI emission. While this may not be true, the resulting kinetic energy would be roughly correct should the energy injection be spherically symmetric. A Gaussian shape is often used for the extrapolation when fitting the mass distribution of observed HI shells (e.g. Giovanelli & Haynes 1979; Koo et al. 1990, 2006). If we adopt this Gaussian extrapolation, (the solid line in Fig. 11), we obtain a value of $1.3 \times 10^4 d_{1.8\text{kpc}}^2 M_{\odot}$. However, this may overestimate the total mass because for an ideal expanding thin shell of uniform density, the mass per unit radial velocity interval is constant. The mass profile at the highest velocities could be decreasing due to the velocity dispersion, or the velocity

structure, within the shell. However, the mass profile at the central velocities would remain constant unless the turbulent velocity in the shell were large enough to be comparable to its expansion velocity.

Here, we develop a simple, but physical, shell model that yields a flat mass profile for the central velocities. We consider a spherical shell with a radius $R = 2^\circ$, a thickness $\Delta R = 10'$, an expansion velocity $v_{\text{exp}} = 55 \text{ km s}^{-1}$, and a dispersion velocity $v_\sigma = 5.5 \text{ km s}^{-1}$. These parameters are derived from the observed HI shell. We assume that the gas density within the shell is constant. For the radial profile of expansion velocity within the shell, we consider two different cases. The first is that the expansion velocity is constant with radius. The second is that the expansion velocity varies linearly with radius. Linearly decreasing or increasing velocity structures within the shell are derived by theoretical studies for different ages of radiative shells (Slavin & Cox 1992; Blondin et al. 1998). Here, we choose a velocity structure for which the expansion velocity at the outer radius drops to 50% of that at the inner radius.

To fit the derived mass distribution, we adopt a three dimensional cube composed of 451^3 pixels. The z axis is along the line of sight (LOS). The number density of HI atoms for a pixel centered at $r = (x^2 + y^2 + z^2)^{1/2}$ is $n(r)$, which is assumed to be constant in our model. This pixel has an LOS velocity $v_{\text{los}}(x, y, z) = v_{\text{exp}}(r)z/r$ where $v_{\text{exp}}(r)$ is the radial expansion velocity at r . The HI 21-cm emission line from this pixel has a Gaussian distribution with the LOS velocity dispersion of $v_\sigma (= 5.5 \text{ km s}^{-1})$. Then the column density, $N(x, y, v)$, at (x, y) over the LSR velocity interval from v to $v + \Delta v$ and the HI mass, $M(v)$, between v and $v + \Delta v$, are given as follows:

$$N(x, y, v) = \frac{n}{\sqrt{2\pi v_\sigma^2}} \int \int_v^{v+\Delta v} \exp \left[\frac{-(v' - v_{\text{los}}(x, y, z))^2}{2v_\sigma^2} \right] dv' dz,$$

$$M(v) = m_{\text{H}} \int \int N(x, y, v) dx dy.$$

The dotted line in Fig. 11 is the best fit for the mass distribution of a shell with a constant expansion velocity profile. Here, the only fitting parameter is the density of the shell. The velocity range, where the mass of the observed HI shell smoothly decreases, is wider than the velocity range due to velocity dispersion, so the observed HI mass distribution cannot be explained by velocity dispersion alone. The dashed line shows the best fit for the mass distribution of a shell with an expansion velocity profile linearly decreasing towards larger radii. This dashed line fits the observed mass better than the dotted line. Variation of the expansion velocity with radius dilutes the rectangular mass distribution at high velocities, but still yields a constant mass distribution at lower velocities, from $v_{\text{LSR}} \sim -50$ to $+10 \text{ km}$

s^{-1} . Note that the basic shape of the mass profile is determined by the difference between the minimum and maximum expansion velocities. The detailed velocity and density structures only affect the shape of the decreasing portion of the mass profile. We will study the mass profiles resulting from various velocity and density structures in a forthcoming paper. The estimated total HI mass of the shell adopting a linearly decreasing velocity profile is $5900d_{1.8\text{kpc}}^2 M_{\odot}$. We will use this value as the characteristic mass of the shell. Note that the total mass derived from the Gaussian fit is about twice this. The kinetic energy of the shell, taking into account the He abundance of 10% by number, is $0.25 \times 10^{51} d_{1.8\text{kpc}}^2$ ergs. The derived physical parameters of the model HI /continuum shell are presented in Table 5.

5.1.2. *The Origin of FVW172.8+1.5 and the X-rays*

We can think of two possibilities for the origin of FVW172.8+1.5; stellar winds from OB stars or SN explosions. HII regions can also produce expanding HI shells, but their expansion velocities and energies are much smaller than those of FVW 172.8+1.5. Furthermore, the HII regions are mostly located at the boundary of the structure, so that they do not appear to be major sources of the 3° – 4° -sized shell. We first consider whether the stellar winds from OB stars can produce FVW172.8+1.5. There are more than a dozen O stars in this area (Garmany et al. 1982; Maiz-Apellaniz et al. 2004) with eight of them projected against the shell (Figs. 5 and 9). We summarize the parameters of these stars in Table 6. Their spectral types range from O9.5 to O7, and four are associated with the Sharpless HII regions. The other four could be possible candidates for the origin of the HI/continuum shell. If we use the relation of Howarth & Prinja (1989) and a wind speed of $\sim 2,000 \text{ km s}^{-1}$, then the typical wind luminosities of O7–O9 main-sequence stars are $(5\text{--}0.8) \times 10^{35} \text{ erg s}^{-1}$. For giant O stars, this would be larger by a factor of two. However, the required wind luminosity to explain the parameters of the shell is $L_w = 77E_K/(9R/v_{\text{exp}}) = 6 \times 10^{37} \text{ erg s}^{-1}$ (Weaver et al. 1977), which is two orders of magnitude greater than the available wind luminosities. Even if there are groups of stars in this area (see next section), their contribution to the wind luminosity will not be significant because they are no brighter than O9.

We thus consider that FVW172.8+1.5 is likely to be the result of an SN explosion. Certainly, the derived parameters are fully consistent with this interpretation. The required SN explosion energy is $E_{\text{SN}} = 6.8 \times 10^{43} n_0^{1.16} R_s^{3.16} v_{\text{exp}}^{1.35} \chi^{0.161}$ ergs, where n_0 is the ambient H density in cm^{-3} , R_s is the radius of the shell in pc, v_{exp} is the expansion velocity in km s^{-1} , and χ is the metallicity in units of the solar metallicity (Cioffi et al. 1988). For the above parameters, $E_{\text{SN}} = 1.3 \times 10^{51}$ ergs, where the solar metallicity has been adopted. This value of E_{SN} is close to the canonical outburst energy of a single SN explosion of 1×10^{51} ergs.

The age of the shell, assuming this to be in the radiative stage of SNR evolution, is $t = 0.3 R_s/v_{\text{exp}} = 0.33$ Myr. The SNR interpretation is also consistent with the presence of X-rays in this region. The thermal energy of the X-ray emitting gas 3×10^{50} ergs, which is 25% of the initial explosion energy and close to that expected for a 0.33 Myr-old radiative SNR (e.g., Cioffi et al. 1988). The apparent segregation between the fast-moving HI gas and the X-ray emitting gas could be due to a non-uniform and/or inhomogeneous density distribution in the ambient medium. It is also possible that more than one SN exploded within the past few 10^5 yr. We have checked for known pulsars in this area, but none are known within the boundary of the putative shell. The nearest pulsar, PSR J0540+32 at $(\ell, b) = (176^\circ 80, +0^\circ 72)$, is $\sim 4^\circ$ distant from the center of the HI/continuum feature, and lies at a distance of ~ 6.2 kpc. PSR J0540+32 is thus unlikely to be associated with the progenitor of FVW172.8+1.5.

5.2. Speculations on the Star-Formation History of G173+1.5

The HII complex G173+1.5 is composed of five Sharpless HII regions S231–235. Of these, all but S234 are clustered around a giant molecular cloud (Fig. 9). There are at least fourteen embedded star-forming clusters that are 3–5 Myr old around these four HII regions (Kirsanova et al. 2008; Dewangan & Anandarao 2011; Camargo et al. 2011, and references therein). S234, located 3° below the other HII regions, also has an associated cluster with young stellar objects having an age of ~ 3 Myr (Jose et al. 2008). It has been proposed that the formation of some of these star-forming clusters could have been triggered by the first-generation stars in these HII regions.

The presence of an old SNR filling the HII complex G173+1.5 has an interesting implication. The five Sharpless HII regions are located within the boundary of the HI/continuum structure, suggesting that their formation could have been triggered by SN explosions, stellar winds, or expanding HII regions from a previous generation of stars (See Elmegreen 1998, for a review of triggered star formation). The age of the SNR for which we have found evidence is, however, only 0.33 Myr, so that it is not possible that the current expanding shell triggered the formation of these HII regions. Instead it could be the cluster to which the SN progenitor belonged that triggered the formation of these HII regions. There are two stellar associations in this area; Aur OB1 at a distance of 1.3 kpc and Aur OB2 at 3.2 kpc (Humphreys 1978). We suspect that Aur OB1, which is scattered over a wide area, ($\ell = 168.^\circ 1\text{--}178.^\circ 1$, $b = -7.^\circ 4\text{--}4.^\circ 2$), could be composed of several associations at slightly different distances. The distance moduli of Aur OB1 stars indeed range from 9.69 to 11.67 or 0.9 to 2.2 kpc in distance (Humphreys 1978). HD 36483 (O9IV) and HD 35921 (O9.5III)

that are relatively close to the central area of the HI/continuum structure also belong to Aur OB1. If one, or both, of these also belonged to the appropriate cluster, then since the main-sequence lifetime of a $20 M_{\odot}$ O9 star is ~ 8 Myr (Schaller et al. 1992), the star formation in this area began about $\gtrsim 8$ Myr ago. In this scenario, the first generation stars triggered the formation of a second generation that are currently exciting the Sharpless HII regions (S231-S235), and we are now observing the formation of third generation stars around these HII regions. The HII complex G173+1.5 could be another good example of sequential star formation over several stellar associations.

6. Summary

We have made high resolution HI 21-cm line observations of a $7^{\circ}5 \times 4^{\circ}5$ area centered at $(\ell, b) = (173^{\circ}, -1.5^{\circ})$ using the ALFA 7-beam receiver mounted on the Arecibo 305 m telescope. The data cube provides a detailed view of the fast-moving HI gas at velocities forbidden by Galactic rotation in this area. FVW 172.8+1.5 is a feature that appears as a faint wing in low-resolution surveys. By comparison with radio continuum, X-ray, and H α maps, we find evidence that FVW 172.8+1.5 is likely to be an old SNR within a large HII complex situated in this area. Our results are summarized as follows:

(1) The HI emission associated with FVW172.8+1.5 is visible from $v_{\text{LSR}} = +19.5$ to $+50.4$ km s^{-1} . At the highest velocities, the HI appears to be separated into two concentrations. At lower velocities a thin, filamentary feature appears surrounding these two concentrations. The increase of the surface area and the amount of HI gas with decreasing velocity suggests that it is an expanding shell. We attribute the complex morphology to the non-uniformity and inhomogeneity of the ambient medium.

(2) The high-velocity HI emission features are confined inside the radio continuum filaments associated with the large HII complex G173+1.5 and show a very good spatial correlation with them. This strongly suggests that it has an origin within the complex. Adopting a distance of 1.8 kpc, and the systemic velocity of -20 km s^{-1} of the HII complex to be appropriate for the HI shell, we derive physical parameters for the shell. These yield a kinetic energy of 2.5×10^{50} ergs. This large kinetic energy and the fast-expansion velocity implies a SN origin.

(3) We investigated the nature of the filaments in HII complex G173+1.5 using multi-wavelength data. Our analysis of the radio continuum spectrum suggests that the radio filaments have both thermal and non-thermal components. A detailed comparison with the associated H α filament supports this conclusion. We also find X-ray emitting hot gas inside

the complex with an estimated thermal energy of 3×10^{50} ergs. This associated hot gas of comparable thermal energy to the kinetic energy of expansion, and the probable presence of non-thermal radio filaments, supports the conclusion that the HV H α gas is of SN origin.

(4) From our analysis, we conclude that FVW 172.8+1.5 is likely to be an old (~ 0.33 Myr) SNR produced inside the HII complex G173+1.5. We propose that the stellar association to which the progenitor belonged could have triggered the formation of the OB stars currently exciting the HII regions. The HII complex G173+1.5 appears to be a potential example of sequential star formation over several stellar associations.

We wish to thank Josh Goldston, Carl Heiles and others who provided enormous help with the observations and data reduction. We are grateful to Min Jin Kim for his help with the continuum data analysis. We thank Tom Dame for kindly providing the CO data cube. Ed Churchwell is thanked for many useful discussions. We also wish to thank the referee, Tom Landecker, for his helpful comments. We would like to thank the staff of the Arecibo Observatory for enormous help with the observations and data reduction. This work has been supported by the Korean Research Foundation under grant KRF-2008-313-C00372 to B.-C. K. The Arecibo Observatory is part of the National Astronomy and Ionosphere Center, which is operated by SRI International under a cooperative agreement with the National Science Foundation (AST-1100968), and in alliance with Ana G. Mndez-Universidad Metropolitana, and the Universities Space Research Association. The Virginia Tech Spectral-Line Survey (VTSS) is supported by the National Science Foundation.

REFERENCES

- Begum, A., Stanimirović, S., Peek, J. E., et al. 2010, *ApJ*, 722, 395
- Beuther, H., Schilke, P., Gueth, F., et al. 2002, *A&A*, 387, 931
- Blitz, L., Fich, M., & Stark, A. A. 1982, *ApJS*, 49, 183
- Blondin, J. M., Wright, E. B., Borkowski, K. J., & Reynolds, S. P. 1998, *ApJ*, 500, 342
- Brogan, C., Gelfand, J. D., Gaensler, B. M. et al., 2006, *ApJ*, 639, L25
- Camargo, D., Bonatto, C., & Bica, E. 2011, *MNRAS*, 416, 1522
- Cioffi, D. F., McKee, C. F., & Bertschinger, E. 1988, *ApJ*, 334, 252
- Dame, T. M., Hartmann, D., & Thaddeus, P. 2001, *AJ*, 547, 792

- Dennison, B., Simonetti, J. H. & Topasna, G. A. 2000, *Bulletin of the American Astronomical Society*, 31, 1455.
- Dewangan, L. K., & Anandarao, B. G. 2011, *MNRAS*, 414, 1526
- Draine, B. T., 2011, *Physics of the Interstellar and Intergalactic Medium* (Princeton; Princeton University Press)
- Elmegreen, B. G. 1998, *ASP Conf. Ser.* 148, *Origins*, ed. C. E. Woodward, J. M. Shull, & H. A. Thronson Jr. (San Francisco: ASP), 150
- Evans, N. J., II, & Blair, G. N. 1981, *ApJ*, 246, 394
- Fich, M., Dahl, G. P., & Treffers, R. R. 1990, *AJ*, 99, 622
- Finkbeiner, D. P. 2003, *ApJS*, 146,407
- Fürst, E., Reich, W., Reich, P., & Reif, K. 1990, *A&AS*, 85, 691
- Gao, X. Y. et al. 2010, *A&A*, 515, 64
- Garmany, C.D., Conti, P.S., & Chiosi, C. 1982, *ApJ*, 263, 777
- Giovanelli, R., & Haynes, M. P. 1979, *ApJ*, 230, 404
- Hartmann, D., & Burton, W. B. 1997, *Atlas of Galactic Neutral Hydrogen*, Cambridge Press
- Heiles, C. 2007, *PASP*, 119, 643
- Heyer, M. H., Carpenter, J. M., & Ladd, E. F. 1996, *ApJ*, 463, 630
- Howarth, I. D., & Prinja, R. K. 1989, *ApJS*, 69, 527
- Humphreys, R. M. 1978, *ApJS*, 38, 309
- Israel, F. P., & Felli, M. 1978, *A&A*, 63, 325
- Jose, J., Pandey, A. K., Ojha, D. K., et al. 2008, *MNRAS*, 384, 1675
- Kang, J.-h., & Koo, B.-C. 2007, *ApJS*, 173, 86
- Kerton, C. R., Murphy, J., & Patterson, J. 2007, *MNRAS*, 379, 289
- Kirsanova, M. S., Sobolev, A. M., Thomasson, M., et al. 2008, *MNRAS*, 388, 729
- Koo, B.-C., & Kang, J.-h. 2004, *MNRAS*, 349, 983

- Koo, B.-C., Reach, W. T., Heiles, C., Fesen, R. A., & Shull, J. M. 1990, *ApJ*, 364, 178
- Koo, B.-C., Kang, J.-h., & Salter, C. J. 2006, *ApJ*, 643, L49
- Landecker, T. L., Reich, W., Reid, R. I., et al. 2010, *A&A*, 520, A80
- Maiz-Apellaniz, J., Walborn, N.R., Galue, H.A., & Wei, L.H. 2004, *ApJS*, 151, 103
- McClure-Griffiths, N. M., Dickey, J. M., Gaensler, B. M., et al. 2005, *ApJS*, 158, 178
- Peek, J. E. G., & Heiles, C. 2008, arXiv:0810.1283
- Peek, J. E. G., Putman, M. E., McKee, C. F., Heiles, C., & Stanimirović, S. 2007, *ApJ*, 656, 907
- Rengelink, R. B., Tang, Y., de Bruyn, A. G., et al. 1997, *A&AS*, 124, 259
- Schaller, G., Schaerer, D., Meynet, G., & Maeder, A. 1992, *A&AS*, 96, 269
- Seward, F. D. 2000, *Allen’s Astrophysical Quantities*, 183
- Sharma, S., Pandey, A. K., Ojha, D. K., et al. 2007, *MNRAS*, 380, 1141
- Sharpless, S. 1959, *ApJS*, 4, 257
- Shepherd, D. S., & Watson, A. M. 2002, *ApJ*, 566, 966
- Slavin, J. D., & Cox, D. P. 1992, *ApJ*, 392, 131
- Snowden, S. L., et al. 1997, *ApJ*, 485, 125
- Spitzer, L. Jr., 1978, *Physical Processes in the Interstellar Medium* (New York; Wiley)
- Stanimirović, S., Putman, M., Heiles, C., et al. 2006, *ApJ*, 653, 1210
- Taylor, A. R., et al. 2003, *AJ*, 125, 3145
- Turtle, A. J., Pugh, J. F., Kenderdine, S., & Pauliny-Toth, I. I. K. 1962, *MNRAS*, 124, 297
- Weaver, R., McCray, R., Castor, J., Shapiro, P., & Moore, R. 1977, *ApJ*, 218, 377

Table 1. Sharpless HII regions in the observed field

Name	RA, Dec (J2000) (h m, ° ')	Diameter ^a (')	$v_{\text{LSR}}^{\text{b}}$ (km s ⁻¹)	$v_{\text{LSR}}^{\text{c}}$ (km s ⁻¹)	Distance ^d (kpc)
S229	5 16.3, +34 27	65	+4.4	+6.7	0.51
S230	5 22.5, +34 08	300	+0.0
S231	5 39.3, +35 56	12	-17.5	-18.1	2.3
S232	5 42.5, +36 12	40	-13.7	-23.0	1.0
S233	5 38.7, +35 48	2	-14.5	-18.4	...
S234	5 28.1, +34 26	12	-14.3	-13.4	2.3
S235	5 41.0, +35 51	10	-25.7	-18.8	1.6
S236	5 22.6, +33 22	55	-3.8	-7.2	3.2
S237	5 31.4, +34 17	7	+1.4	-4.3	1.8

^aOptical size (Sharpless 1959)

^bH α emission line radial velocity (Fich et al. 1990)

^cCO radial velocity (Blitz et al. 1982). For S229, the association is uncertain.

^dDistance determined by spectrophotometry of the central exciting star. See the references in Blitz et al. (1982).

Table 2. Parameters of the continuum surveys used for spectral analysis

Name	Frequency (MHz)	Resolution	RMS (mK)	References
WENSS	325	54 " \times 54 " csc δ	2300	Rengelink et al. (1997)
CGPS	408	2 '8 \times 2 '8 csc δ	950	Taylor et al. (2003)
CGPS	1420	49 " \times 49 " csc δ	68	Taylor et al. (2003)
Effelsberg 11-cm	2695	4'3	20	Fürst et al. (1990)

Table 3. Integrated radio continuum flux densities of Filament A and S232

	325 MHz (Jy)	408 MHz (Jy)	1420 MHz (Jy)	2695 MHz (Jy)	Spectral index ($S \propto \nu^{-\alpha}$)
Filament A	1.5 ± 0.17	0.84 ± 0.14	0.87 ± 0.03	0.73 ± 0.05	$+0.23 \pm 0.06$
S232	1.8 ± 0.07	1.9 ± 0.10	1.9 ± 0.10	2.2 ± 0.05	-0.09 ± 0.02

Note. — The areas used for the flux density measurements of the filament A and S232 are indicated in Fig. 7.

Table 4. Spectral indices from T-T plots

	325-1420 MHz	325-2695 MHz	408-1420 MHz	408-2695 MHz
Filament A	$+0.50 \pm 0.11$	$+0.32 \pm 0.06$	$+0.07 \pm 0.10$	-0.04 ± 0.08
S232	$+0.09 \pm 0.07$	-0.00 ± 0.04	$+0.06 \pm 0.04$	-0.04 ± 0.02

Table 5. Parameters for an expanding shell

Parameter	Estimated value
Center (α, δ)	$05^{\text{h}}33^{\text{m}}29^{\text{s}}, +35^{\circ}50'52''$
(ℓ, b)	$172^{\circ}.78, +1^{\circ}.51$
Mean radius	$69 \times 54 d_{1.8\text{kpc}}$ pc
Expansion velocity	55 ± 5 km s $^{-1}$
Total HI mass	$5900 \pm 770 d_{1.8\text{kpc}}^2 M_{\odot}$
Kinetic energy	$0.25 \pm 0.05 \times 10^{51} d_{1.8\text{kpc}}^2$ ergs
Initial ISM density	$0.25 \pm 0.03 d_{1.8\text{kpc}}^{-1}$ cm $^{-3}$
Age	0.33 ± 0.03 Myr

Note. — The errors are 1σ errors. For the estimation of the initial ISM density and age, we use the geometrical average of the mean radius (61 pc).

Table 6. O-type stars within the HII complex G173+1.5

Name	RA, Dec (J2000) (h m, ° ')	Spectral Type	Distance (kpc)	Associated HII Region
HD 36483	5 33.8, +36 28	O9IV	1.3	...
HD 35921	5 29.8, +35 20	O9.5III	1.3	...
LS V+35 24	5 39.7, +35 53	O9V	2.1	S231
BD +35 1201	5 41.0, +35 50	O9.5V	1.6	S235
HD 37737	5 42.4, +36 09	O9.5III	1.3	S232
BD +34 1058	5 28.4, +34 40	O8	3.2	...
HD 35619	5 27.5, +34 47	O7V	3.2	...
BD +34 1054	5 28.1, +34 25	O9.5V	2.0	S234

Note. — The O stars (Garmany et al. 1982; Maiz-Apellaniz et al. 2004) located within a radius of $2^{\circ}5$ from the center of the HI/continuum structure are listed in order of angular distance from the center. See also Fig. 5. The distance of a star is computed from its distance modulus, assuming an interstellar absorption of $A(V)=3E(B-V)$ (Garmany et al. 1982).

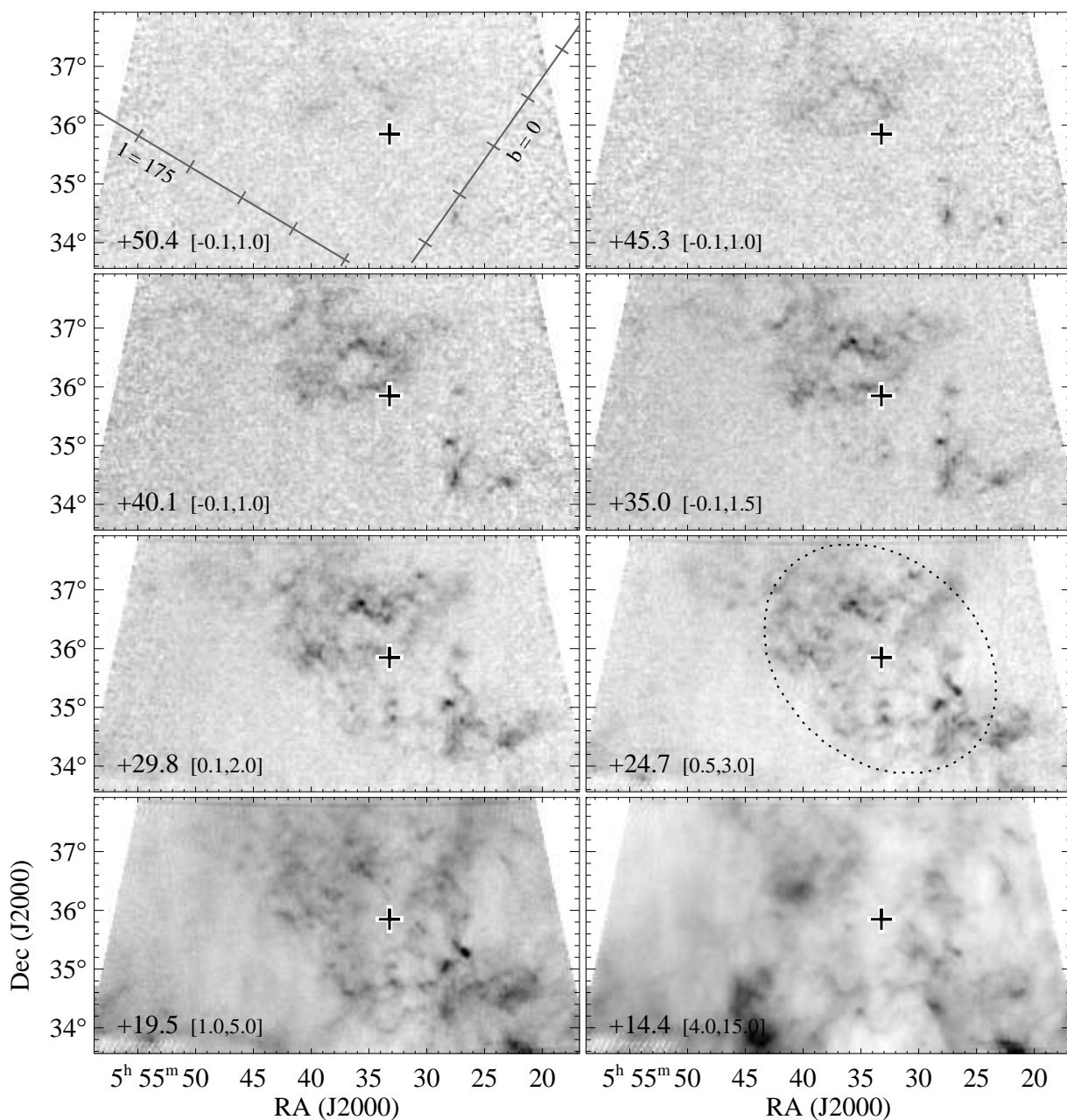


Fig. 1.— HI channel images of the observed field. Each image is integrated over a velocity interval of 5.1 km s^{-1} . The central LSR velocity is given at the bottom left of each image. The numbers in the brackets are the minimum and maximum brightness temperatures (K) of the grey scale which is linear. The black cross indicates the approximate center of the HI structure. The dotted ellipse on the $+24.7 \text{ km s}^{-1}$ frame marks the boundary of the proposed shell as adopted in this paper.

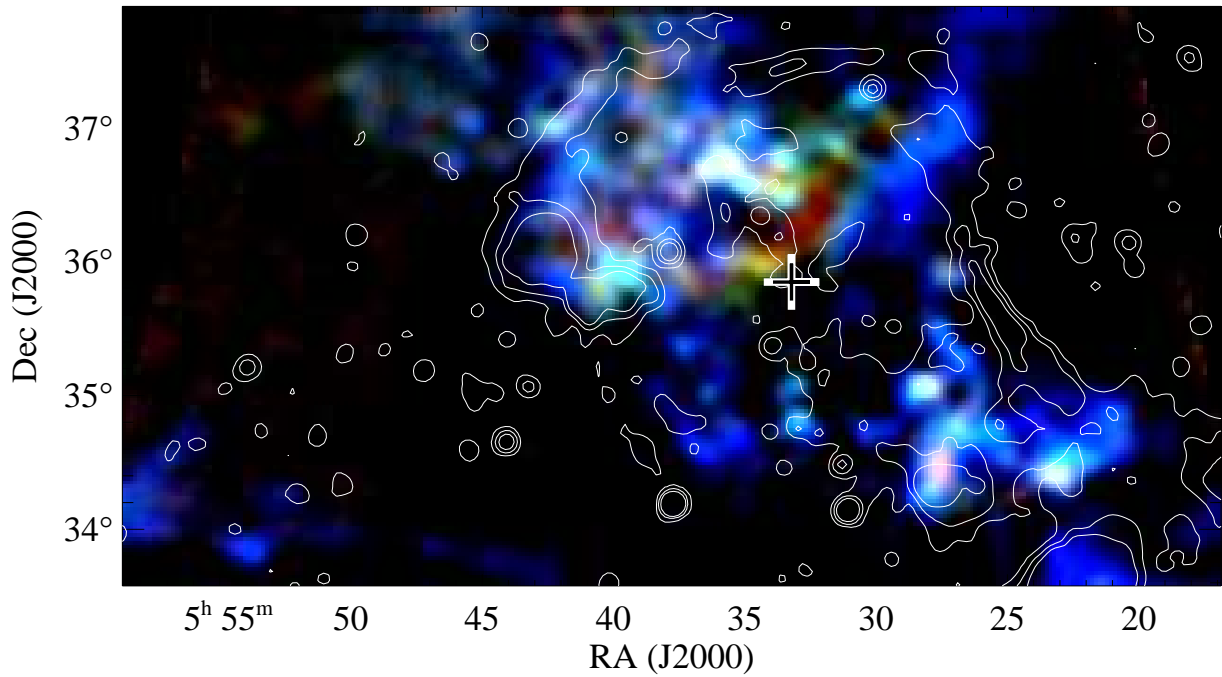


Fig. 2.— A three-color image showing the Arcibo HI emission from FVW172.8+1.5. Red, green, and blue represent the images integrated over LSR velocities of +45 to +35, +35 to +25, and +25 to +20 km s⁻¹ respectively. Effelsberg 11-cm radio continuum contours (Fürst et al. 1990) are overplotted. Contour levels are 30, 100, 200 mK in brightness temperature.

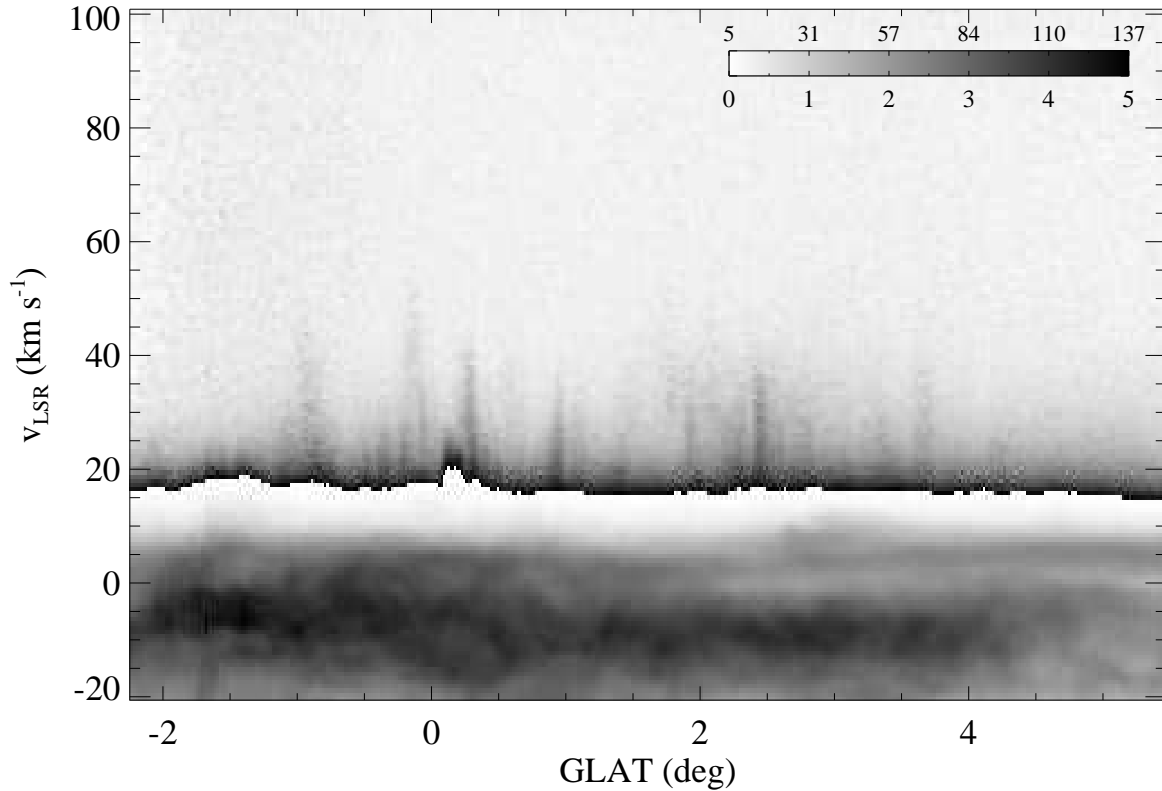


Fig. 3.— The HI peak brightness temperature over the range of Galactic longitude, $171.^{\circ}8$ to $173.^{\circ}7$, as a function of Galactic latitude. In order to show HI features at lower velocities, the intensity scale for brightness temperatures in excess of 5 K is greatly expanded. The grey-scale ranges are shown by the bar in the upper right of the figure; values for brightness temperatures < 5 K are marked below the bar, with those for > 5 K are marked above. The merit of a peak intensity image is that it enhances bright structures that would not be seen in an averaged image.

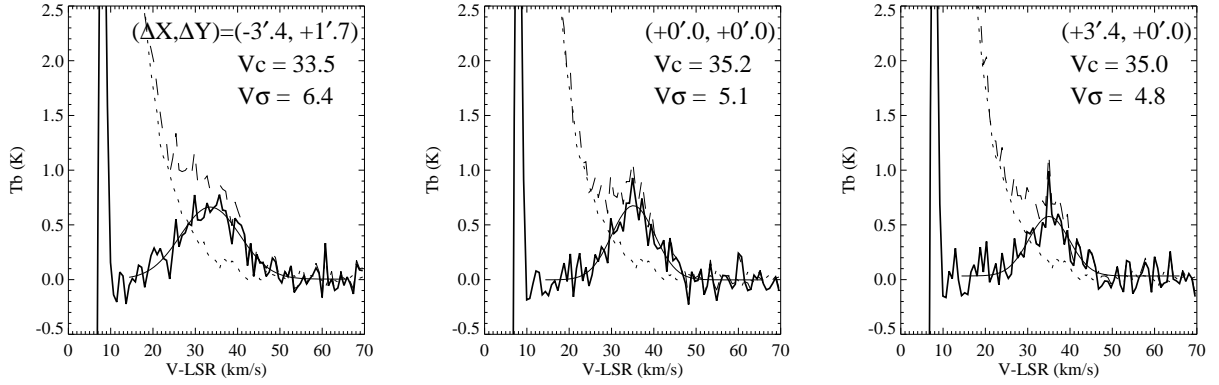


Fig. 4.— Sample line profiles in the area around ($5^{\text{h}} 34.5^{\text{m}}, +36^\circ 03'$). The relative positions are shown in each frame. Dashed and thick solid lines show the original and background-subtracted line profiles, respectively. The thin solid lines show the best fit of Gaussian profiles to the background-subtracted profiles. The central velocities and velocity dispersions of the Gaussians in km s^{-1} are given in each frame.

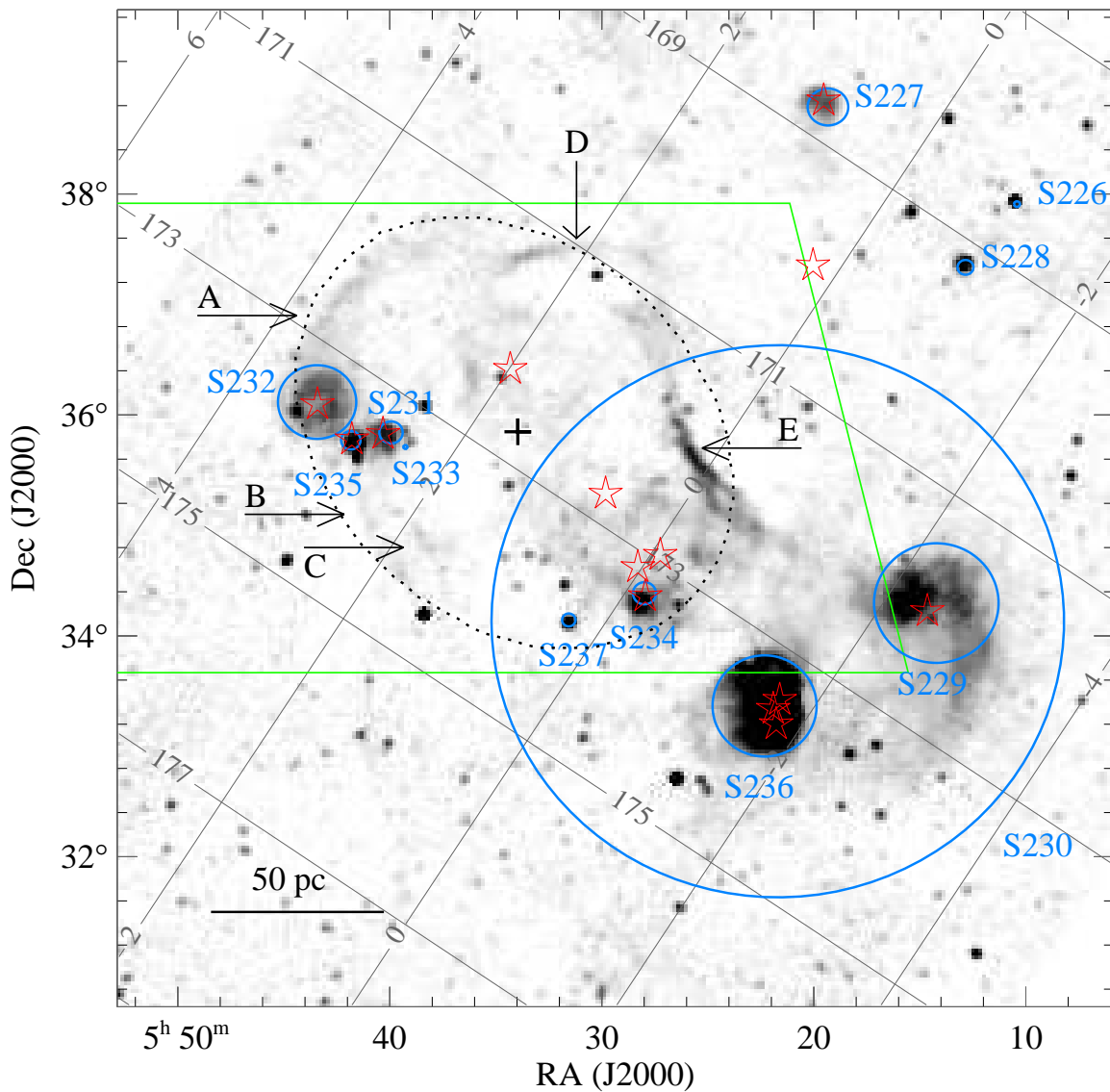


Fig. 5.— A grey-scale plot of the Effelsberg 11-cm radio continuum in the direction of FVW172.8+1.5. Sharpless HII regions are marked by blue circles, while Galactic O stars are marked by red star symbols. The region observed at Arecibo (Fig. 1) is shown by green lines. The black cross and the dotted ellipse are the approximate center and boundary adopted for the shell, respectively. The continuum filaments defining the HII complex are marked by arrows. The scale bar in the bottom left represents 50 pc at 1.8 kpc.

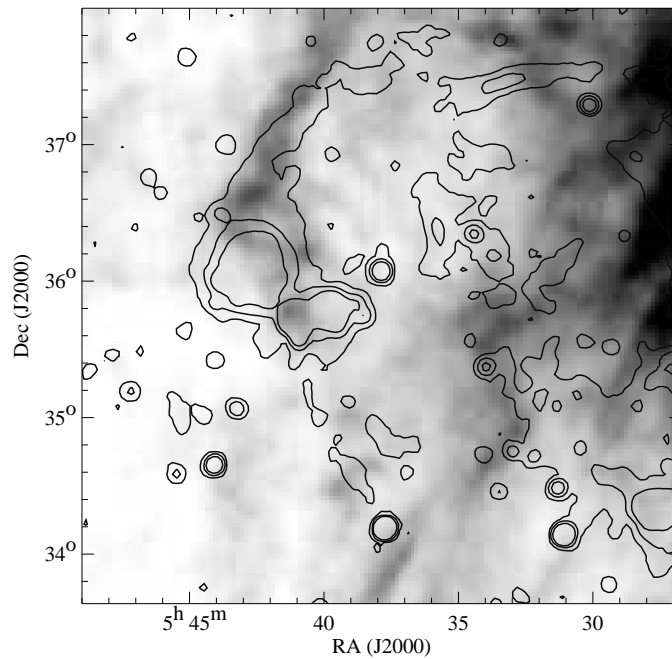


Fig. 6.— An HI map integrated from $v_{\text{LSR}} = -28$ to -25 km s^{-1} , with the 11-cm continuum contours overlaid. An HI filament along the continuum filament A is visible (cf. Fig. 5), although the correlation is not perfect.

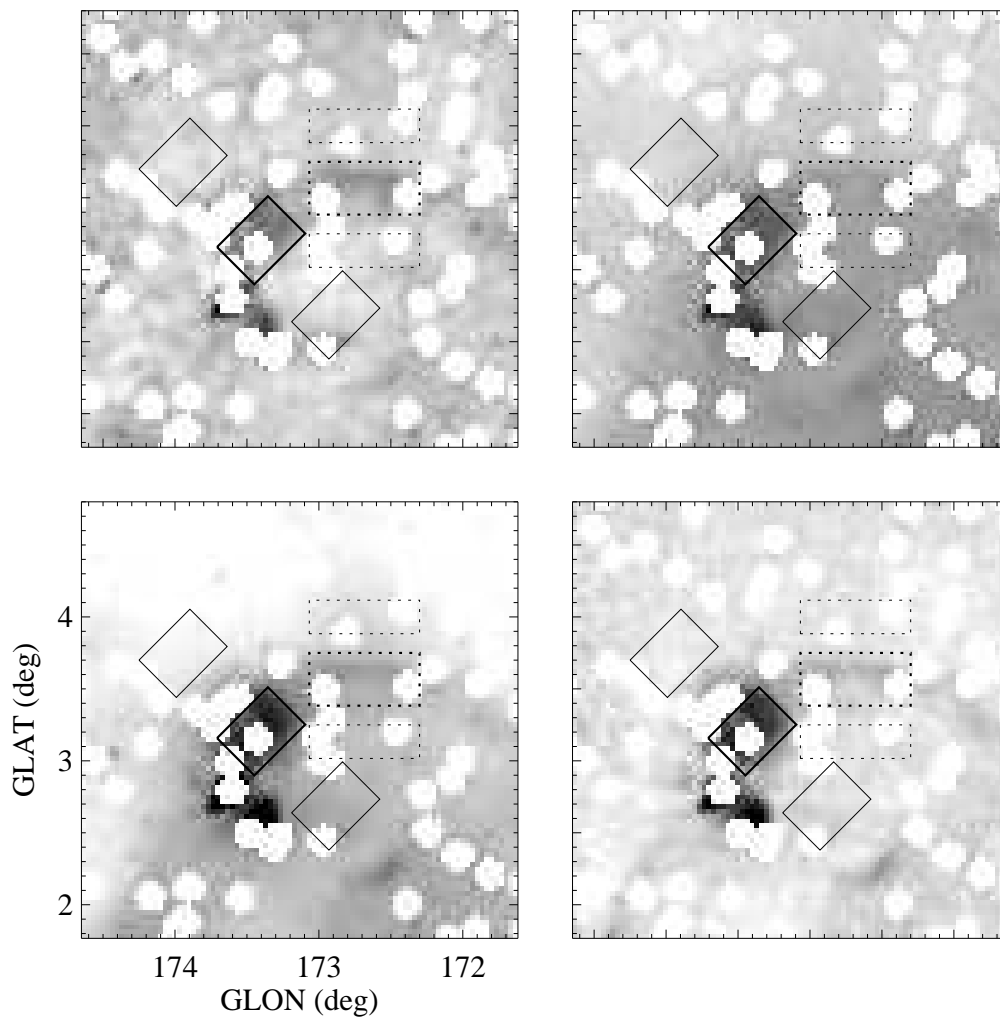


Fig. 7.— WENSS 325 MHz (top left), CGPS 408 MHz (top right), CGPS 1420 MHz (bottom left), and Effelsberg 2695 MHz (bottom right) radio continuum images of the northern part of the FVW173+1.5 field. The areas used to derive the total flux density and to plot T-T diagrams of radio continuum filament A and the HII region, S232, are marked by thick dotted and solid boxes, respectively. The neighboring areas used for the subtraction of the large scale background are marked by thin dotted and solid boxes. The white holes in the images are where point sources have been subtracted.

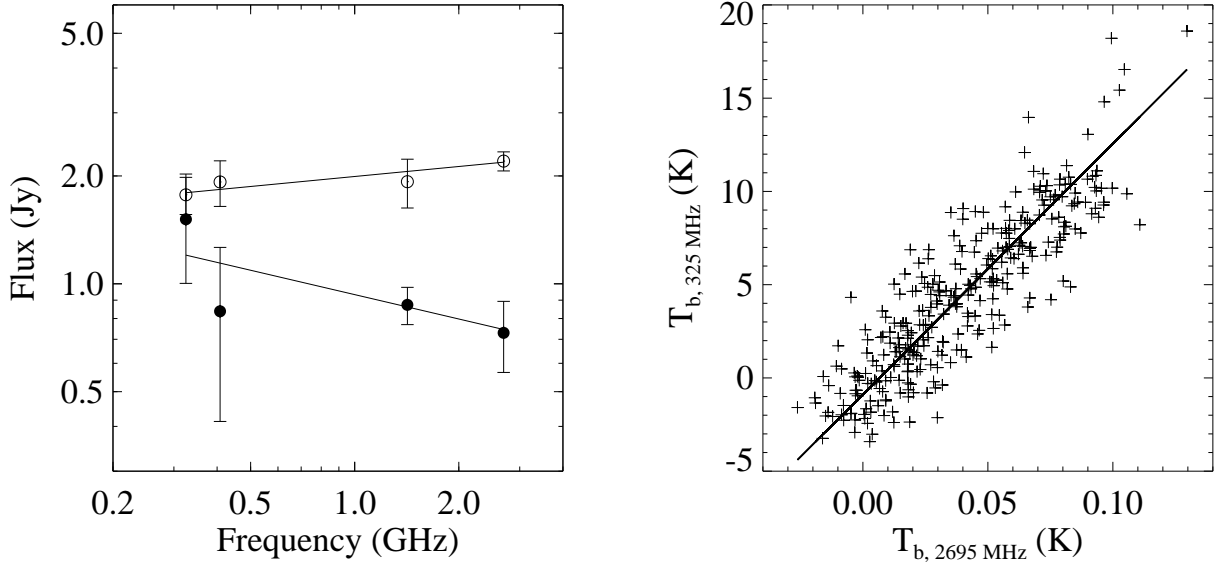


Fig. 8.— (Left) Flux densities of the HII region S232 (open circles) and the continuum filament A (filled circles). The fitted spectra, with α ($S \propto \nu^{-\alpha}$) = -0.09 ± 0.02 and $+0.23 \pm 0.06$ for the HII region and filament respectively, are overplotted. (Right) The T-T plot for the area of filament A using the WENSS 325 MHz and Effelsberg 2695 MHz data. The best linear fit with $\alpha = +0.32 \pm 0.06$ is overplotted.

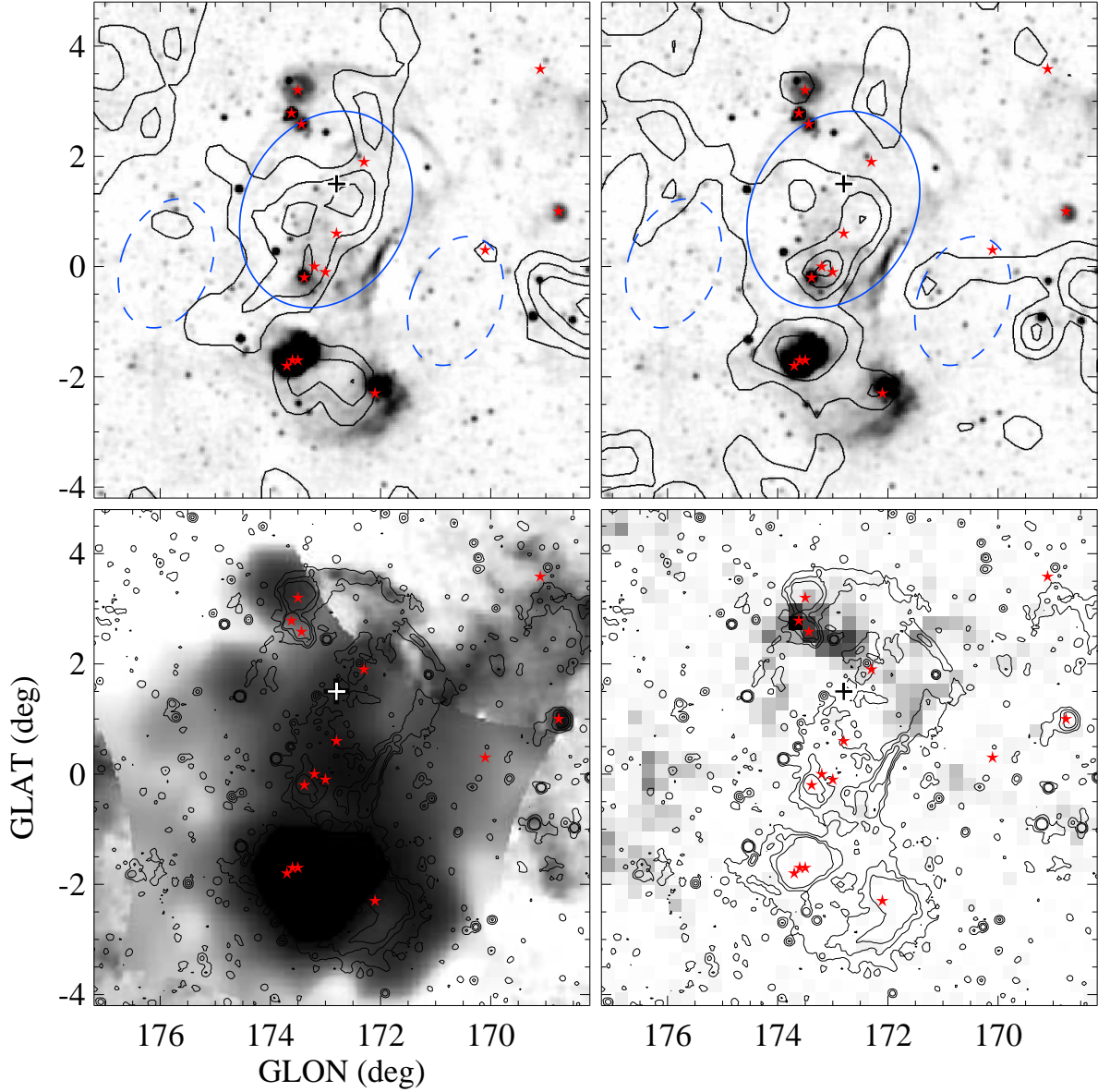


Fig. 9.— (Top left) The ROSAT R45 (3/4 keV) band diffuse X-ray contour map overlotted on the Effelsberg 11-cm image. The contour levels are 70, 85, and 100 in counts $s^{-1} \text{ arcmin}^{-2}$. (Top right) As for the top left frame, but for the ROSAT R67 (1.5 keV) band. The contour levels are 100, 120, 140, and 160 in counts $s^{-1} \text{ arcmin}^{-2}$. (Bottom left) The $H\alpha$ map (6' FWHM resolution) composite from the Virginia Tech Spectral line Survey (VTSS) and the Wisconsin H-Alpha Mapper survey (Finkbeiner 2003). The scale for the image is 40 – 70 Rayleigh, but a histogram equalization method is performed to enhance the contrast of the H-alpha filaments. (Bottom right) CO J=1-0 intensity image integrated over $v_{\text{LSR}} = -25$ to -15 km s^{-1} . The scale for the image is 0 – 0.3 K, and is linear. The blue ellipses in solid and dotted lines overlotted on the top two images are the area used to measure the X-ray counts of the shell and the backgrounds, respectively. The O stars are marked by red stars.

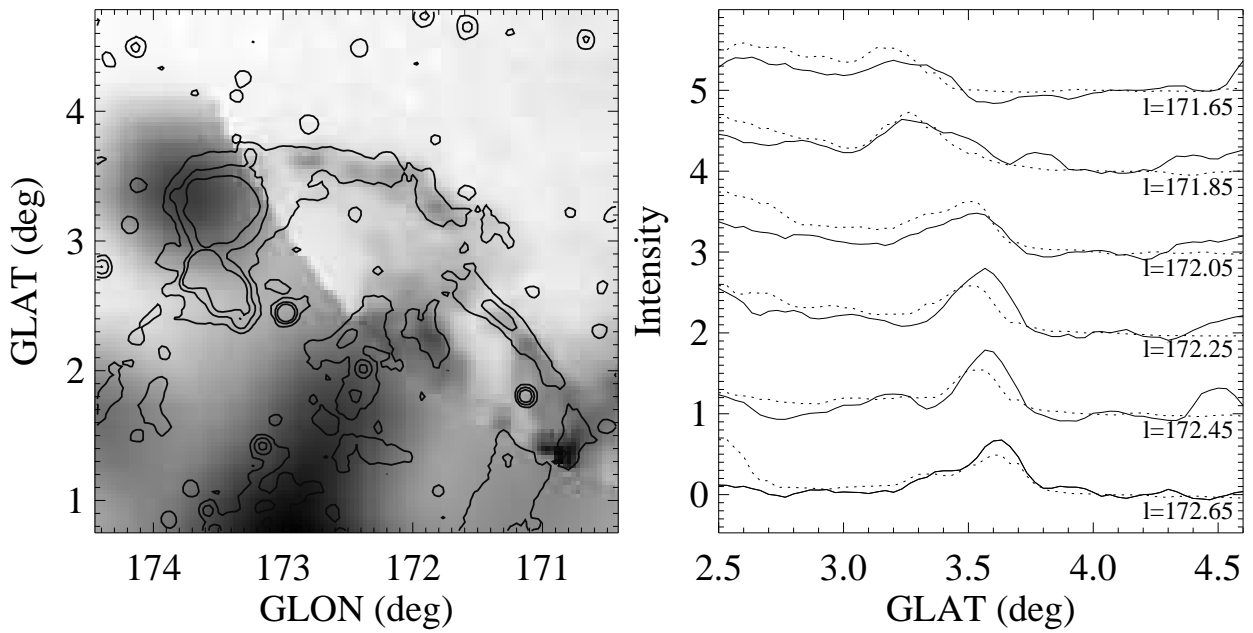


Fig. 10.— (Left) An enlarged view of the filament A in the VTSS H α image with the 11-cm radio continuum contours superposed. (Right) One-dimensional intensity distributions of H α (dotted lines) and 11-cm continuum (solid lines) emission along Galactic latitudes at several Galactic longitudes. H α and continuum intensities are normalized by 20 R and 0.1 K, respectively.

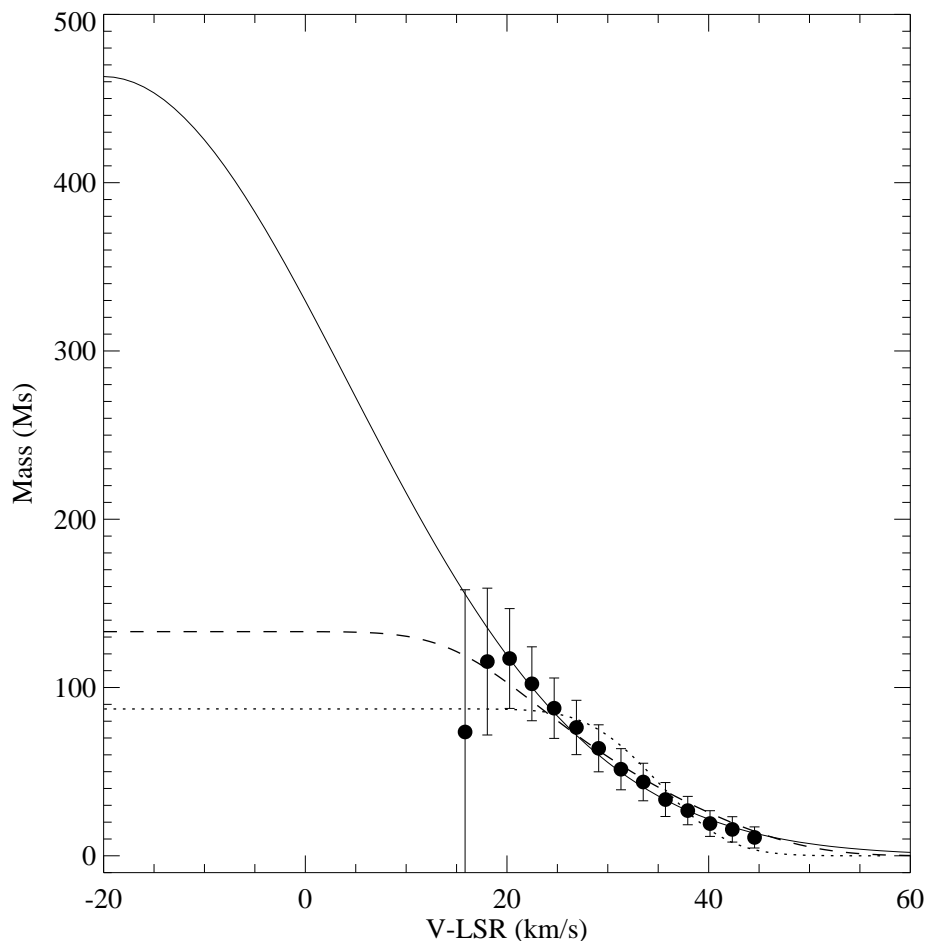


Fig. 11.— The mass distribution for the putative HI shell assuming a distance of 1.8 kpc. The filled circles are the derived HI masses for each 2.2 km s^{-1} velocity interval. The error bars show the standard deviation for the background area. The solid line shows a Gaussian fit to the data, while the dotted line shows the best fit for the mass distribution of a shell with a constant $v_{\text{exp}} = 55 \text{ km s}^{-1}$ and $v_{\sigma} = 5.5 \text{ km s}^{-1}$, and the dashed line shows the best fit for the mass distribution of a shell with a velocity dispersion $v_{\sigma} = 5.5 \text{ km s}^{-1}$, but whose expansion velocity at the outer radius of the shell drops linearly to 50% of the expansion velocity at the inner radius.